Title

Variable flip angle balanced steady-state free precession for lower SAR or higher contrast cardiac cine imaging

Journal

Magnetic Resonance in Medicine, 71(3)

ISSN

0740-3194

Authors

Srinivasan, Subashini
Ennis, Daniel B

Publication Date

2014-03-01

DOI

10.1002/mrm.24764

Peer reviewed

Magnetic Resonance in Medicine 71:1035–1043 (2014)

Variable Flip Angle Balanced Steady-State Free Precession for Lower SAR or Higher Contrast Cardiac Cine Imaging

Subashini Srinivasan[1,2] and Daniel B. Ennis[1,2,3]*

Purpose: Cardiac cine balanced steady-state free precession (bSSFP) imaging uses a high flip angle (FA) to obtain high blood-myocardium signal-to-noise and contrast-to-noise ratios (CNR). Use of high FAs, however, results in substantially increased SAR. Our objective was to develop a variable FA bSSFP cardiac cine imaging technique with: (1) low SAR and blood-myocardium CNR similar to conventional constant FA bSSFP (CFA-bSSFP) or (2) increased blood-myocardium CNR compared to CFA-bSSFP with similar SAR.

Methods: Variable FA bSSFP cardiac cine imaging was achieved using an asynchronous k-space acquisition, which is asynchronous to the cardiac cycle (aVFA-bSSFP). Bloch simulations and phantom experiments were performed to compare the signal, resolution, and frequency response of the variable FA bSSFP and CFA-bSSFP schemes. Ten volunteers were imaged with different aVFA-bSSFP and asynchronous CFA-bSSFP schemes and compared to conventional segmented CFA-bSSFP.

Results: The SAR of aVFA-bSSFP is significantly decreased by 36% compared to asynchronous CFA-bSSFP (1.9 ± 0.2 vs. 3.0 ± 0.2 W/kg, $P < 10^{-10}$) for similar blood-myocardium CNR (34 ± 6 vs. 35 ± 9, $P = 0.5$). Alternately, the CNR of the aVFA-bSSFP is improved by 28% compared to asynchronous CFA-bSSFP (49 ± 9 vs. 38 ± 8, $P < 10^{-4}$) with similar SAR (3.2 ± 0.5 vs. 3.3 ± 0.5 W/kg, $P = 0.6$).

Conclusion: aVFA-bSSFP can be used for lower SAR or higher contrast cardiac cine imaging compared to the conventional segmented CFA-bSSFP imaging. **Magn Reson Med 71:1035–1043, 2014. © 2013 Wiley Periodicals, Inc.**

Key words: variable flip angle balanced steady-state free precession; cardiac cine imaging; low SAR imaging

Cardiac cine imaging is routinely performed clinically using balanced steady-state free precession (bSSFP) (1) (i.e., TrueFISP, b-FFE, and FIESTA) due to its high blood-myocardium contrast-to-noise ratio (CNR) and high signal-to-noise ratio (SNR) efficiency. The blood-myocardium CNR for spoiled gradient echo imaging technique strongly depends on inflow, which can result in low blood-myocardium CNR, especially in patients with impaired cardiac function. The SNR in bSSFP is dependent on the T_2^*/T_1 values of the tissues. Due to the inherent differences in T_2^*/T_1 values between myocardium and blood, bSSFP imaging provides higher CNR, even for patients with impaired myocardial function. The bSSFP blood SNR also increases with increasing flip angle (FA) (2) due to the dependence of the blood signal on in-flow velocity and out of slice effects (2). The use of higher FAs with a short repetition time (TR), however, results in substantially increased specific absorption rate (SAR in W/kg), which limits achievable SNR and CNR and can restrict the use of bSSFP for applications such as imaging patients with implanted devices (e.g., pacemakers and implantable cardioverter defibrillators (ICD)) and imaging at higher field strengths ($\geq$3 T).

Variable flip angle (VFA) imaging approaches have been developed to lower SAR for spin echo imaging (3,4), to obtain T_2-weighted contrast with bSSFP (5) or steady-state free precession (SSFP)-echo (6) sequences, to increase spatial resolution for bSSFP imaging (7); and to increase SNR in bSSFP (8) and spoiled gradient echo (9) noncine imaging. All of these techniques have used single-shot imaging or multishot imaging, but without application to cardiac cine imaging, which is conventionally acquired using segmented cine k-space acquisitions.

Conventional k-space segmented cardiac cine bSSFP images (Fig. 1a) acquire the first k-space segment for each cardiac phase during the first cardiac cycle (RR-interval) followed by the acquisition of the second segment for each cardiac phase during the second cardiac cycle and so on until all k-space segments are acquired. However, various VFA schemes coupled to segmented k-space acquisitions and bSSFP are not able to reduce the overall SAR of the sequence efficiently and produce significant image artifacts (see Methods).

We propose to use an asynchronous k-space acquisition (Fig. 1b) for variable FA bSSFP (VFA-bSSFP) cardiac cine imaging, which is asynchronous to the cardiac cycle, termed as aVFA-bSSFP. This is equivalent to acquiring multiple single-shot images of the same slice and retrospectively rebinning the data based on the phase of the cardiac cycle. Kellman et al. previously used a similar asynchronous k-space acquisition for high resolution free-breathing cardiac cine imaging (10) in order to uniformly sample the k-space during different cardiac phases.

Therefore, our *objective* was to develop the aVFA-bSSFP technique specifically for cardiac cine imaging. We *hypothesize* that the aVFA-bSSFP technique can: (1) lower the SAR of cardiac cine bSSFP imaging while

[1]Department of Bioengineering, University of California, Los Angeles, California, USA.

[2]Department of Radiological Sciences, University of California, Los Angeles, California, USA.

[3]Biomedical Physics Interdepartmental Program, University of California, Los Angeles, California, USA.

*Correspondence to: Daniel B. Ennis, Ph.D., Peter V. Ueberroth Building, Suite 1471, Room B, 10945 Le Conte Avenue, Los Angeles, CA 90095. E-mail: daniel.ennis@ucla.edu

Received 14 December 2012; revised 18 March 2013; accepted 20 March 2013

DOI 10.1002/mrm.24764

Published online 29 April 2013 in Wiley Online Library (wileyonlinelibrary.com).

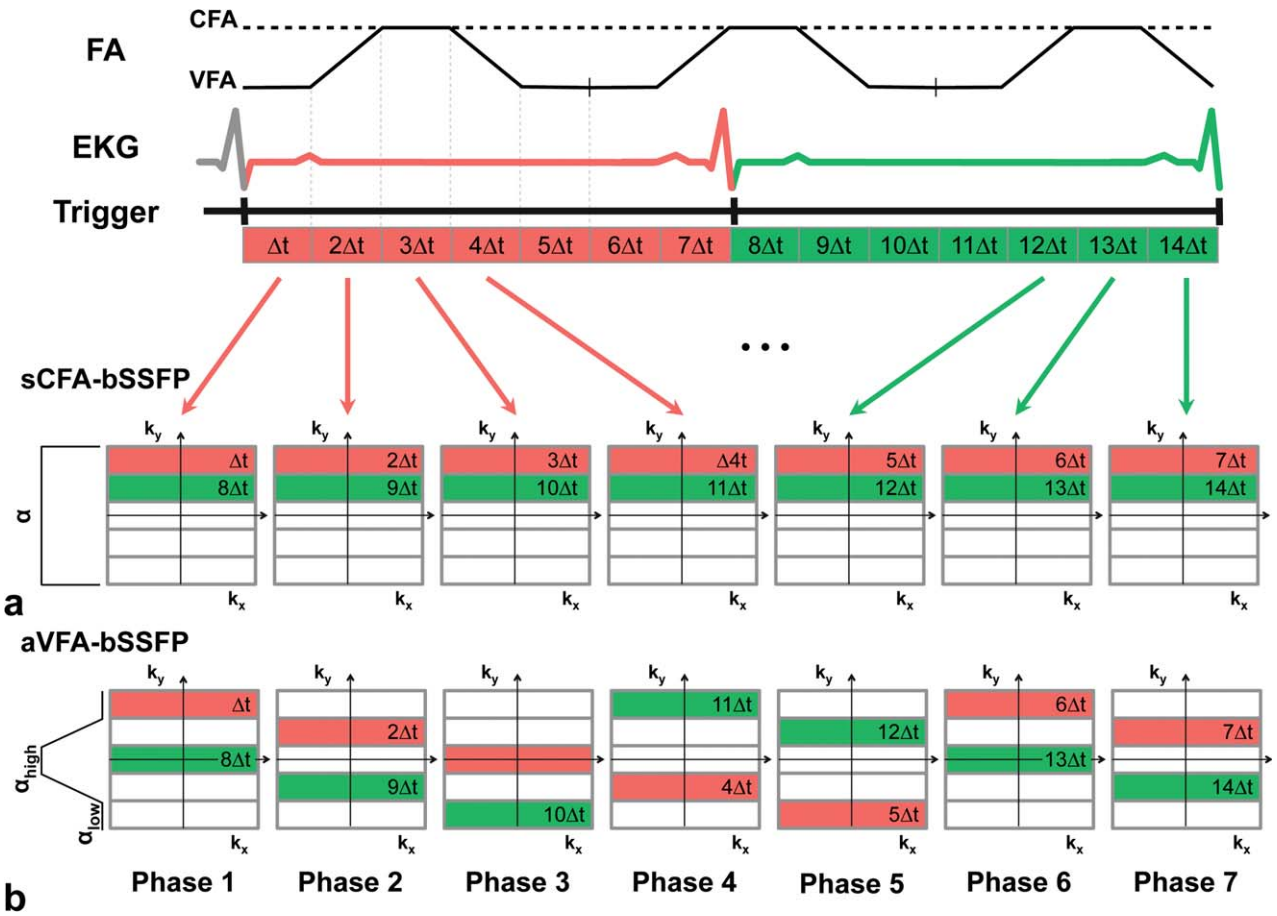

FIG. 1. Comparison of conventional segmented k-space acquisition (**a**) to the asynchronous VFA-bSSFP cardiac cine technique (**b**) showing the k-space acquisition of seven cardiac phases during the first two RR-intervals (red and green). The VFA-bSSFP scheme is asynchronous to the RR-interval as shown on the top. Δt, $2\Delta t$, and so on indicate the acquisition order of the different segments, where Δt is the acquisition duration for each segment. The VFA-bSSFP scheme varies from α_{low} to α_{high} and back to α_{low} linearly across k-space, which reduces the SAR, while maintaining image contrast.

maintaining blood-myocardium CNR similar to conventional segmented constant FA bSSFP (sCFA-bSSFP) or (2) increase the blood SNR and blood-myocardium CNR compared to asynchronous constant FA bSSFP (aCFA-bSSFP) with similar SAR.

METHODS

Design of FA Scheme for VFA-bSSFP

The proposed VFA scheme uses a trapezoidal FA history (3) which is defined by five different parameters: a low FA (α_{low}), a high FA (α_{high}), the number of α_{low} pulses (N_{low}), the number of linear ramp pulses (N_{ramp}), and the number of α_{high} pulses (N_{high}) as shown in Figure 2. The combination of these parameters is defined as the number of VFA (N_{VFA}) $= 2 \times N_{low} + 2 \times N_{ramp} + N_{high}$. The proposed VFA scheme is designed such that $N_{VFA} = N_{ky}$, where N_{ky} is the number of phase encode steps per shot. Images are acquired using a top-down trajectory such that α_{high} is used to acquire the center of k-space, thereby maintaining the overall SNR and CNR of the image to be similar to conventional bSSFP. The α_{low} pulses accord with the outer k-space lines, and therefore, reduce the overall SAR of the image acquisition, but concomitantly incur a loss in resolution too. The linear N_{ramp} pulses promote a smooth transition between the lower (α_{low}) and higher (α_{high}) steady states, which minimizes

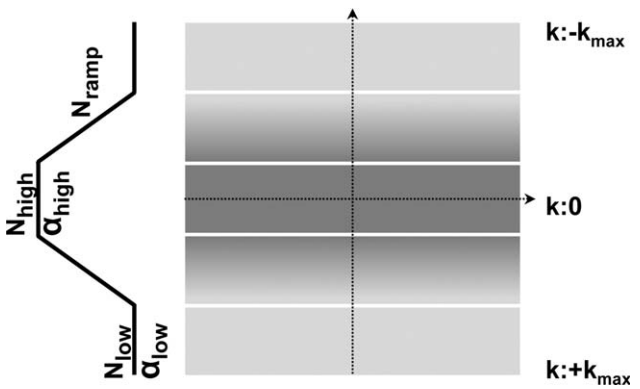

FIG. 2. VFA-bSSFP uses a trapezoidal FA scheme consisting of five different parameters: lower FA (α_{low}), higher FA (α_{high}), number of low pulses (N_{low}), number of high pulses (N_{high}), and number of linear ramp pulses (N_{ramp}). The α_{low} pulses are used to acquire the outer k-space lines to reduce the SAR, followed by the ramp pulses to catalyze a smooth transition to a higher steady state that uses α_{high} for increased SNR.

Table 1
Twenty-Five Different VFA-bSSFP and CFA-bSSFP Schemes Used for Simulations and Imaging Experiments

	$\alpha_{high} = 50^\circ$	$\alpha_{high} = 70^\circ$	$\alpha_{high} = 90^\circ$
$\alpha_{low} = 10^\circ$	10_50_20_40	10_70_20_40	**10_90_20_40**
	10_50_40_40	10_70_40_40	**10_90_40_40**
	10_50_20_80	**10_70_20_80**	
	10_50_40_80	**10_70_40_80**	
		10_70_60_80	
		10_70_20_100	
		10_70_40_100	
$\alpha_{low} = 30^\circ$	30_50_20_40	**30_70_20_40**	
	30_50_40_40	**30_70_40_40**	
	30_50_20_80	**30_70_20_80**	
	30_50_40_80	**30_70_40_80**	
$\alpha_{low} = 50^\circ$	CFA-bSSFP 50	**50_70_20_40**	
		50_70_40_40	
$\alpha_{low} = 70^\circ$		**CFA-bSSFP 70**	

The VFA-bSSFP schemes in nonbold were used to determine the scheme with blood-myocardium CNR similar to CFA-bSSFP of 50° and bold VFA-bSSFP schemes were used to determine the scheme with blood-myocardium CNR similar to CFA-bSSFP of 70°. The VFA-bSSFP scheme is represented as $\alpha_{low}\_\alpha_{high}\_N_{ramp}\_N_{high}$.

artifacts. Throughout this article, a specific VFA scheme is represented as $\alpha_{low}\_\alpha_{high}\_N_{ramp}\_N_{high}$. For example, VFA scheme 30_70_40_80 is used to represent the scheme with $\alpha_{low} = 30^\circ$, $\alpha_{high} = 70^\circ$, $N_{ramp} = 40$, and $N_{high} = 80$. For a fixed, N_{ky} (e.g., $N_{ky} = 204$) we then have $N_{low} = [N_{ky} - (N_{high} + 2 \times N_{ramp})]/2 = 22$. For comparison purposes, we also evaluated aCFA-bSSFP sequence that uses the same asynchronous acquisition and reconstruction technique as aVFA-bSSFP.

Twenty-five different aVFA-bSSFP and aCFA-bSSFP schemes (Table 1) were evaluated with simulations and imaging experiments to determine which aVFA-bSSFP scheme produced blood-myocardium CNR similar to aCFA-bSSFP of 50° and 70° while reducing SAR and with minimal loss in resolution. The schemes were chosen systematically by varying the VFA-bSSFP scheme parameters: α_{low} was varied from 10° to α_{high} in steps of 20°, N_{ramp} was chosen as 20 or 40, N_{high} was either 40, 80, or 100, and α_{high} was 50°, 70°, or 90°. Only VFA-bSSFP schemes with ΣFA^2 (proportional to the SAR of the sequence for a fixed TR) lower than the corresponding constant FA bSSFP (CFA-bSSFP) sequence were chosen.

VFA Acquisition Strategy

Various VFA-bSSFP acquisition strategies could be used with a segmented k-space acquisition in order to reduce SAR, but the concomitant artifacts, poor blood-myocardium contrast, and minimal SAR reduction makes each approach unfavorable. For example, the acquisition strategy could vary the FA throughout the RR-interval such that $N_{VFA} = N_{segments}$ (number of k-space lines acquired within each segment) $\times N_{phases}$ (number of cardiac phases). However, the center of k-space for the middle cardiac phase would be acquired with a higher FA and consequently would have higher CNR and SNR, and the center of k-space for the first and last cardiac phases would be acquired with a lower FA and would have a lower SNR and CNR. This difference in SNR and CNR between cardiac phases is undesirable. Alternately, the FA could vary across each k-space segment such that $N_{VFA} = N_{segments}$, but N_{VFA} would be small and consequently would not significantly reduce the SAR, and the concomitant signal modulations in the k-space would cause artifacts. Lastly, if the FA was varied over the entire imaging acquisition such that $N_{VFA} = N_{segments} \times N_{phases} \times$ number of cardiac cycles, the images would have ghosting artifacts due to k-space discontinuities that arise as a consequence of rebinning the data acquired during the ramp interval.

To overcome the above problems, we propose using an asynchronous k-space acquisition with $N_{VFA} = N_{ky}$ for VFA-bSSFP, where k-space is filled asynchronously with respect to the RR-interval. In each RR-interval, consecutive continuous segments that span all cardiac phases are acquired without synchronization to the cardiac cycle. The asynchronous k-space acquisition is also equivalent to acquiring multiple single-shot images, which are retrospectively rebinned into different cardiac phases. The asynchronous acquisition is unlike the conventional segmented acquisition, where the same k-space segment is acquired for all the cardiac phases in each RR-interval. Figure 1 compares the segmented and asynchronous k-space acquisitions during the first two RR-intervals. An asynchronous k-space acquisition with $N_{VFA} = N_{ky}$, avoids the above-mentioned limitations (i.e., ghosting, CNR fluctuations, and ineffective SAR reductions), because a continuous k-space acquisition of the different cardiac phases with the consecutive trapezoidal VFA schemes not susceptible to ghosting artifacts, maintains similar SNR and CNR during all the cardiac phases and significantly reduces the SAR.

Bloch Equation Simulations

Bloch equation simulations were performed in MATLAB (The Mathworks, Natick, MA). Simulations of the transverse magnetization (M_{xy}) as a function of the echo number were performed for stationary myocardium (T_1/T_2: 867/57 ms), flowing blood ($T_1/T_2/T_2^*$: 1200/200/200 ms), and an aqueous nickel-sulfate phantom (T_1/T_2: 100/100 ms). Both a conventional CFA-bSSFP sequence of 70° and a 30_70_40_80 VFA-bSSFP scheme were simulated. An imperfect slice profile was simulated with 20 subslices (N_s) and a 600 μs RF pulse with a time bandwidth product of 1.6 similar to Markl et al. (2). The slice profile was defined by the Fourier transform of the RF pulse. The slice profile was divided into 20 subslices, and the FA for each subslice was defined by scaling the subslice's signal by the central subslice's signal. The other simulation parameters were spin density of the myocardium (M_{0myo}) = 0.7, (M_{0blood}) = 0.95 (11), pulse repetition time (TR) = 3.070 ms, echo time (TE) = 1.535 ms, number of shots (N_{shots}) = 5, and $N_{ky} = 204$. The flow simulation follows the previous work of Markl et al. (2) with a percent spin replacement per TR (Δs) of 50% and a number of out-of-slice subslices, $N_{os} = 4 \times \Delta s \times N_s \times T_2/TR$.

Simulations of the myocardial signal and flowing blood signal were also performed for the 25 different VFA-bSSFP and CFA-bSSFP schemes (Table 1) with the same simulation parameters explained above. The simulated myocardial and flowing blood signal was calculated as the dynamic steady-state signal of the center echo number from the third shot. The resolution loss incurred by the VFA-bSSFP scheme was estimated for each of the 25 different FA schemes. The point spread function (PSF) was calculated as the Fourier transform of the dynamic steady-state signal of the third shot. The full width half max (FWHM) of the PSF was measured as the width of the PSF at half the maximum value to estimate the resolution loss.

The frequency response of the 30_70_40_80 VFA-bSSFP scheme and a 70° CFA-bSSFP scheme was simulated by calculating the signal for the phantom (T_1/T_2: 100/100 ms) with off-resonance between −180° and 180° in 5° steps.

Imaging Experiments

All the images were acquired on a 1.5 T scanner (Avanto; Siemens Medical Solutions, Erlangen, Germany) using a 6-channel anterior cardiac coil and 6-channel posterior spine matrix.

Phantom Imaging

A nickel-sulfate phantom (1.25 g of $NiSO_4 \times 6\ H_2O$ + 5 g NaCl per 1000 g of distilled water) was imaged using multiecho spin-echo experiments to measure T_2 with TR = 8000 ms and TE = 11, 50, 100, 150, and 200 ms. The T_1 values were measured using multiple inversion recovery spin-echo experiments. The imaging parameters were: TR = 4000 ms, TE = 9.5 ms, and inversion time (TI) = 10, 50, 75, 100, 120, 200, 300, 400, 500, 1000, 1500, and 3000 ms. The values were estimated to be T_1/T_2:100/100 ms by fitting the signal curves. The phantom was imaged with parameters matched to the simulations (field of view = 380×302 mm, acquisition matrix = 256×204, resolution = $1.5 \times 1.5 \times 5$ mm, TE/TR = 1.535/3.070 ms, bandwidth = 1502 Hz/px, and $N_{shots} = 25$), and VFA-bSSFP scheme (30_70_40_80). Projections were acquired with the phase encoding gradients switched-off in order to evaluate the dynamics of the transverse magnetization with high temporal resolution. The sum of the coil combined signal (using sum of squares technique) along the readout direction was compared to the simulated results.

Resolution phantom experiments were performed on a phantom with different sized disks to qualitatively compare the image sharpness acquired with VFA-bSSFP (30_70_40_80) and CFA-bSSFP (70°). Images of the plastic grid in the American College of Radiology (ACR) MRI accreditation phantom (J M specialty parts, San Diego, CA) were also acquired using the 25 different bSSFP schemes (Table 1). To quantify image blurriness, the first two shots were discarded and the subsequent images from 23 consecutive shots were averaged to reduce the noise. The blurriness of a single edge of the grid was measured at three different locations similar to Larson et al. (12) by first measuring I_{max} and I_{min} (maximum and minimum image intensity) points on a line profile drawn over the grid along the phase encoding direction, then computing the distance between 0.8 $(I_{max} - I_{min}) + I_{min}$ and 0.2 $(I_{max} - I_{min}) + I_{min}$. The imaging parameters were identical to the stationary phantom experiment.

The frequency response of the CFA-bSSFP (70°) and VFA-bSSFP (30_70_40_80) schemes was experimentally measured by applying a linear shim gradient of 200 μT/m along the readout direction using the nickel-sulfate phantom with imaging parameters identical to the above experiments. The line profile over the phantom was compared to the simulated frequency response.

In Vivo Imaging

A 2D breath-hold cardiac cine exam was performed in 10 normal subjects ($N = 10$, 8 males, age: 28 ± 4 years) subsequent to obtaining informed written consent. Our Institutional Review Board approved the protocol. 2D midventricular short-axis cardiac cine exams were performed using sCFA-bSSFP with FAs of 50° and 70° ($N_{segments} = 16$ and $N_{phases} = 25$). The other imaging parameters were identical to the phantom experiments mentioned above. Twenty-five different experiments (Table 1) for the same midventricular short-axis slice were acquired with each bSSFP schemes in each volunteer.

The ECG signal was recorded during image acquisition for offline reconstruction of the aVFA-bSSFP and aCFA-bSSFP images. The acquisition duration for both the aVFA-bSSFP and aCFA-bSSFP experiments was 15 s. The acquisition duration for the sCFA-bSSFP acquisitions depended on the heart rate variation during the image acquisition and averaged 12 ± 2 s.

2D short-axis cardiac cine images were also acquired using aCFA-bSSFP with the maximum FA based on the individual patient's SAR limit. A aVFA-bSSFP scheme (50_α_{high}_40_40, where α_{high} was 98 ± 1°) with SAR approximately matched to patient-specific SAR for aCFA-bSSFP ($\alpha = 74 \pm 5°$) was also acquired in order to evaluate the potential increase in blood-myocardium CNR using aVFA-bSSFP compared to aCFA-bSSFP with similar SAR.

Image Reconstruction

The aVFA-bSSFP and aCFA-bSSFP images were reconstructed offline retrospectively, using MATLAB. The first shot consisted of significant signal transients during the approach to steady-state and was discarded during image reconstruction. Subsequently, each k-space line was associated with a normalized time (between 0 and 1) based on its time-of-acquisition with respect to the corresponding RR-interval (cardiac cycle) obtained from the ECG data. Each k_y-line was then linearly interpolated into 25 cardiac phases, coil combined (sum of squares), 2D Fourier transformed, and the magnitude resulted in 25 cardiac cine images.

In Vivo Data Analysis

The SNR of the blood and myocardium was measured using region of interest (ROI) analysis. ROIs were drawn over the septum and left ventricular blood of the single-shot diastolic images and the mean signal was measured.

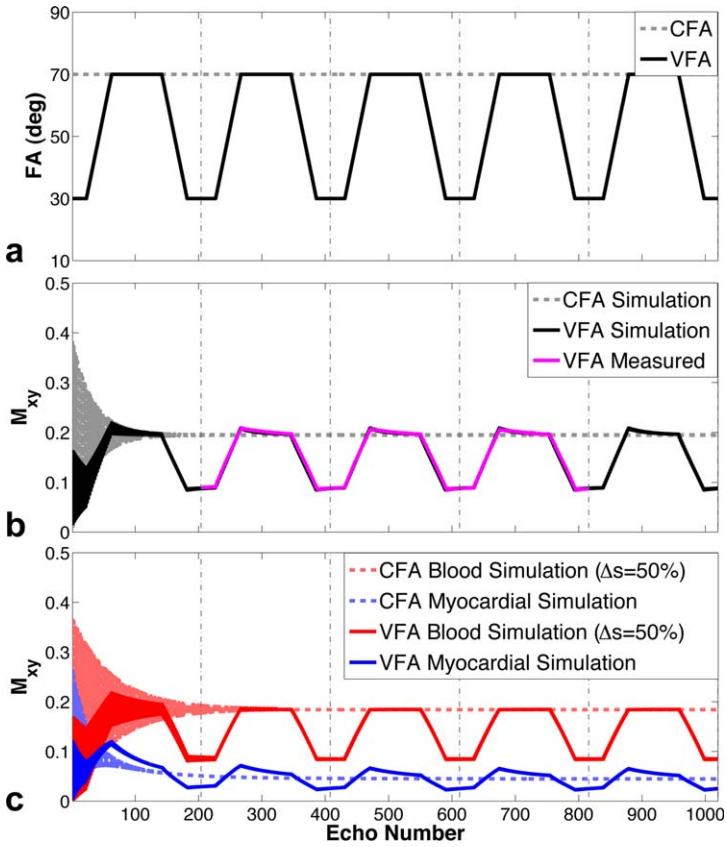

FIG. 3. (a) The FA scheme for the CFA-bSSFP (70°) and VFA-bSSFP (30_70_40_80). The measured and simulated **(b)** transverse magnetization (phantom $T_1/T_2 = 100/100$ ms) for the CFA-bSSFP (dashed line) and VFA-bSSFP (solid line) schemes are shown. The simulations and measurements confirm that after approximately 150 echoes CFA-bSSFP transverse magnetization reaches a steady-state, whereas VFA-bSSFP transverse magnetization results in a dynamic steady-state. In **(c)** simulations of stationary myocardium (T_1/T_2:867/57 ms) and flowing blood (T_1/T_2:1200/200 ms, Δs: 50%) for both CFA-bSSFP and VFA-bSSFP are shown. [Color figure can be viewed in the online issue, which is available at wileyonlinelibrary.com.]

The interpolated images were not used for this analysis to avoid any complex impact on the measured signal and noise. The standard deviation of the background noise was also measured. SNR was calculated as the ratio of the mean signal to the standard deviation of the noise. Blood-myocardium CNR was calculated as the ratio of signal difference of blood and myocardium to the standard deviation of the noise. A paired student's *t*-test was performed to test for significant differences between the mean blood-myocardium CNR and SAR values obtained for the aVFA-bSSFP and aCFA-bSSFP experiments.

Comparison of the Bloch Simulation and Measured Data

The experimentally measured values were scaled to best fit the simulation results based on linear least squares fit between all the simulations and mean experimental data. This was performed for the following experiments: (1) simulation vs. measured signal phantom; (2) simulation vs. measured frequency response; and (3) comparison of the simulated blood and myocardial signal and measured blood and myocardial SNR. The correlation coefficient (R) was calculated between the simulated and the mean of the measured experimental data.

RESULTS

Simulations and Phantom Experiments

The FA schemes for the simulation and phantom experiments of VFA-bSSFP and CFA-bSSFP are shown in Figure 3a. The simulation of the transverse magnetization for the phantom using the VFA-bSSFP and CFA-bSSFP (Fig. 3b), demonstrates the repeated dynamic steady-state signal using the VFA-bSSFP scheme and the constant signal of the CFA-bSSFP scheme after the first ~150 echoes. The measured signal obtained from the nickel-sulfate phantom agrees well ($R = 0.99$) with the simulation confirming the accurate simulation of the dynamic steady-state signal (Fig. 3b). Simulation of the myocardium and flowing blood signals for the VFA scheme (Fig. 3c) demonstrate a consistent dynamic steady state signal after the first single-shot measurement (Fig. 3a). The duration of the transverse magnetization signal transient (time to reach steady-state) is slightly shorter using the 30_70_40_80 VFA-bSSFP scheme compared to CFA-bSSFP scheme.

Dynamic steady-state (third shot) resolution phantom images (Fig. 4a–d) show that both the VFA-bSSFP and CFA-bSSFP schemes have similar sharpness for low-resolution objects (Fig. 4e). However, the smaller objects appear slightly blurred for VFA-bSSFP (30_70_40_80) compared to CFA-bSSFP (70°) due to the modulation of signal across k-space (Fig. 4f). SAR, however, is also decreased by 36% (0.49 vs. 0.76 W/kg). The simulation results show that the FWHM is increased 30% for the VFA-bSSFP scheme compared to CFA-bSSFP (1.3 vs. 1.0) as shown in Figure 5a. The simulation of the FWHM of the PSF and phantom measurements of the mean image blurriness measured from the line profile (Fig. 5c) along the phase encoding direction (Fig. 5a,b) agree well ($R = 0.91$) for the 25 different VFA-bSSFP experiments.

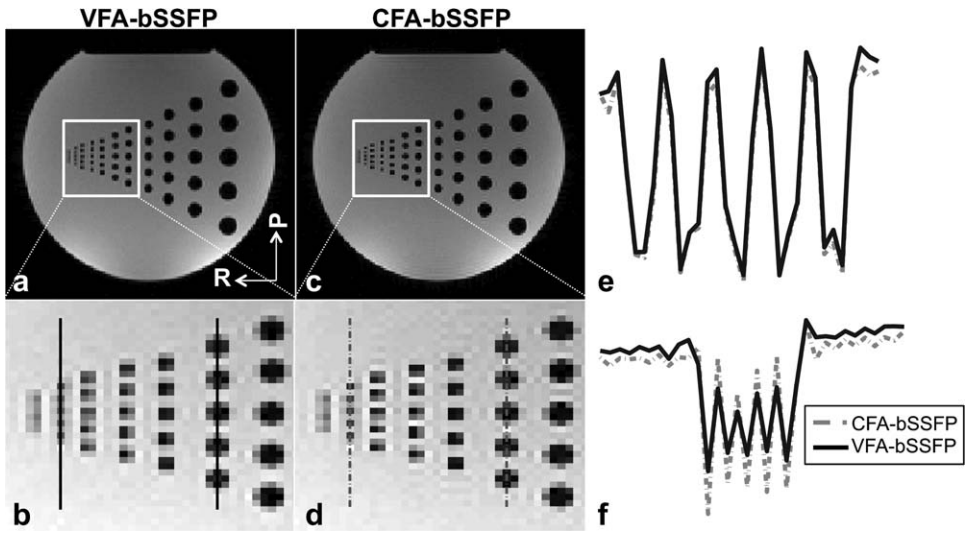

FIG. 4. Dynamic steady state resolution phantom images acquired with 30_70_40_80 VFA-bSSFP (**a**) scheme and CFA-bSSFP of 70° (**c**). The corresponding zoomed images are shown in (**b**) and (**d**) with line profiles drawn over the sixth (**e**) and second (**f**) row (from left to right) of the resolution phantom for VFA-bSSFP (black solid line) and CFA-bSSFP (gray-dashed line). The phase encoding (P) and the readout (R) axes are labeled.

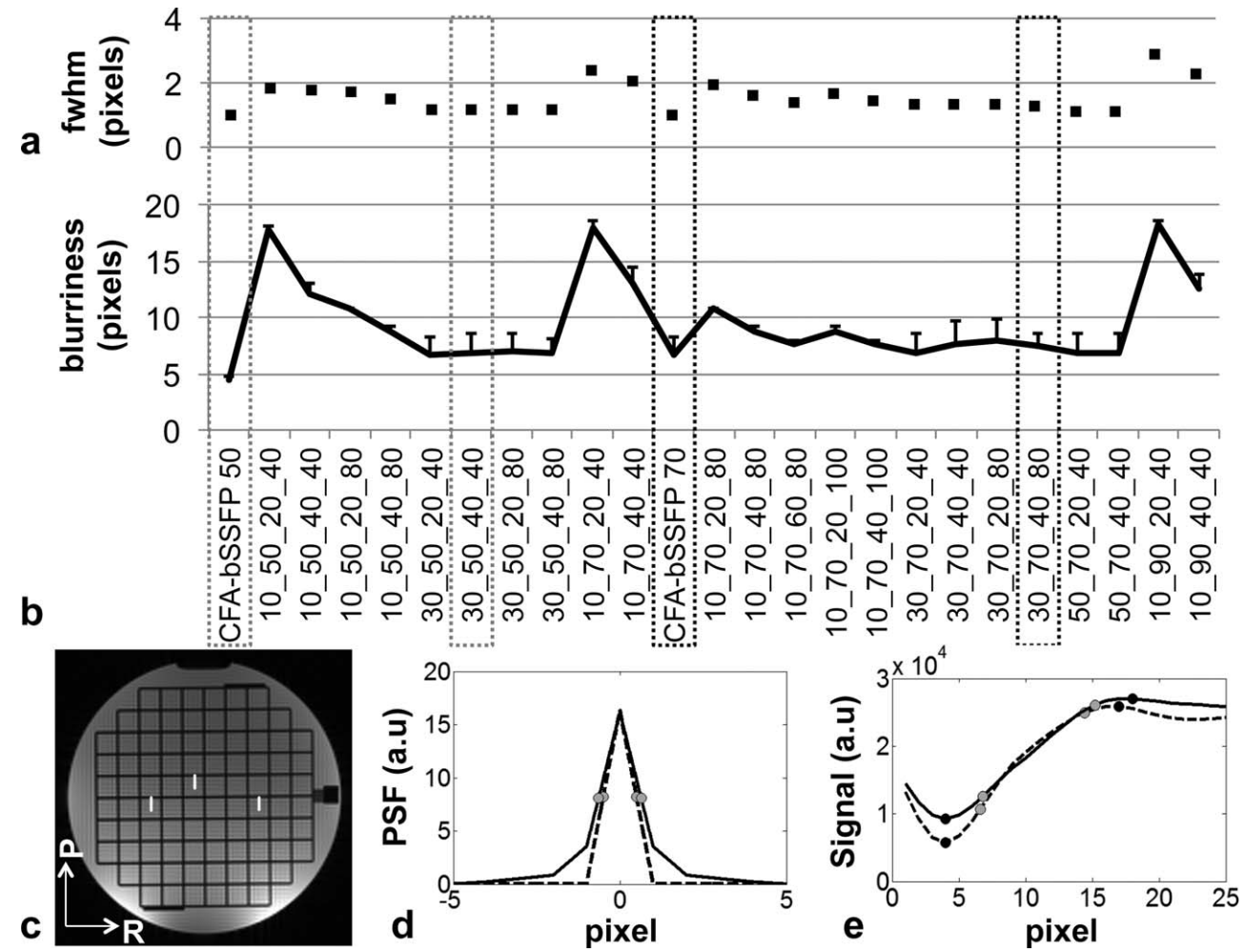

FIG. 5. Simulated FWHM of the PSF (**a**) and the mean of the measured image blurriness (**b**) over a line profile (**c,** solid white lines) of the phantom along the phase encoding direction agrees well for the 25 different experiments. The phase encoding (P) and the readout (R) axes are labeled. The black dotted rectangles highlight the comparison of the CFA-bSSFP 70° with its corresponding 30_70_40_80 VFA-bSSFP scheme. The gray-dotted rectangles highlight the comparison of CFA-bSSFP 50° and its corresponding 30_50_40_40 VFA-bSSFP scheme. Example simulations of the PSF of CFA-bSSFP 70° (dashed line) and 30_70_40_80 VFA-bSSFP (solid line) are shown in (**d**) and the corresponding line profile drawn over the center solid line are shown in (**e**).

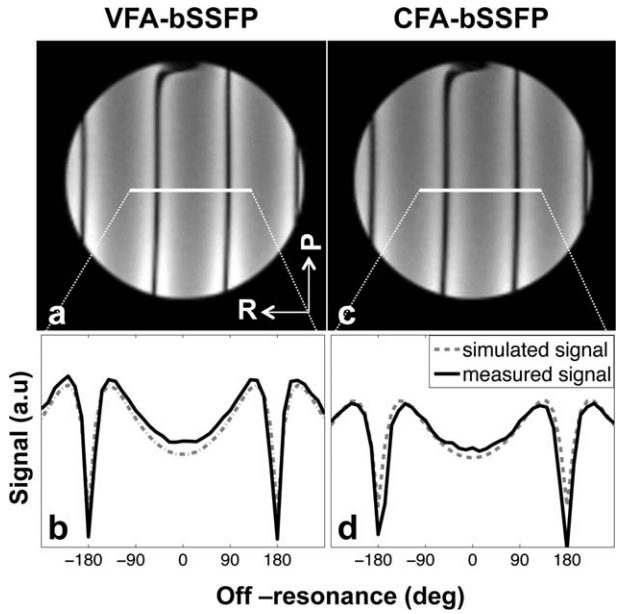

FIG. 6. Phantom images acquired with an additional gradient of 200 μT/m along the readout direction for 30_70_40_80 VFA-bSSFP (**a**) scheme and CFA-bSSFP of 70° (**c**). Simulated frequency profiles (solid line) and measured line profiles (dashed line) are shown for VFA-bSSFP (**b**) and CFA-bSSFP (**d**). The phase encoding (P) and the readout (R) axes are labeled.

Example images showing the simulated PSF of 70° CFA-bSSFP and 30_70_40_80 VFA-bSSFP are shown (Fig. 5e), and the line profiles drawn in the phantom images are also shown (Fig. 5f) for the corresponding acquisitions.

The phantom experiments during application of the additional linear gradient shows that the VFA-bSSFP scheme has banding artifacts at multiples of 1/TR similar to the CFA-bSSFP scheme (Fig. 6a,c). The measured line profile and simulated frequency profiles (Fig. 6b,d) agree well ($R = 0.93$).

In Vivo Analysis

Diastolic and systolic images acquired in a normal subject with sCFA-bSSFP (FA = 70°), aCFA-bSSFP of 70°, and aVFA-bSSFP (30_70_40_80) are shown in Figure 7. The SAR of aVFA-bSSFP compared to aCFA-bSSFP is significantly decreased by 36% (1.9 ± 0.2 vs. 3.0 ± 0.2 W/kg, $P < 10^{-10}$) for similar blood-myocardium CNR (34 ± 6 vs. 35 ± 9, $P = 0.5$). The SAR and blood-myocardium CNR of the sCFA-bSSFP were similar to aCFA-bSSFP experiments (3.0 ± 0.3 W/kg, 35 ± 7). Figure 8 shows diastolic and systolic images acquired in a normal subject using the maximum (SAR limited) aCFA-bSSFP of 70° and aVFA-bSSFP (50_98_40_40). The blood-myocardium CNR of the aVFA-bSSFP compared to aCFA-bSSFP is improved by 28% (49 ± 9 vs. 38 ± 8, $P < 10^{-4}$) with similar SAR (3.2 ± 0.5 vs. 3.3 ± 0.5 W/kg, $P = 0.6$).

Figure 9 compares the simulated myocardial signal and the simulated flowing blood signals to the in vivo mean myocardial SNR and blood SNR in 10 subjects for the 25 different aVFA-bSSFP and aCFA-bSSFP experiments. The error bars show the standard deviation of these values in 10 volunteers. The mean and standard deviation of the SAR of each of these sequences is also indicated. The simulated signal and measured SNR of the myocardium ($R = 0.95$) and blood ($R = 0.98$) agree well.

DISCUSSION

aVFA-bSSFP can be used for low SAR cardiac cine imaging with similar myocardial and blood SNR and blood-myocardium CNR compared to the conventional sCFA-bSSFP sequence with minimal loss in image resolution. This may prove especially useful for imaging exams wherein SAR is a concern (patients with implanted devices and real time imaging). aVFA-bSSFP can also be used to improve the blood-myocardium CNR compared to the CFA-bSSFP with similar SAR, because it

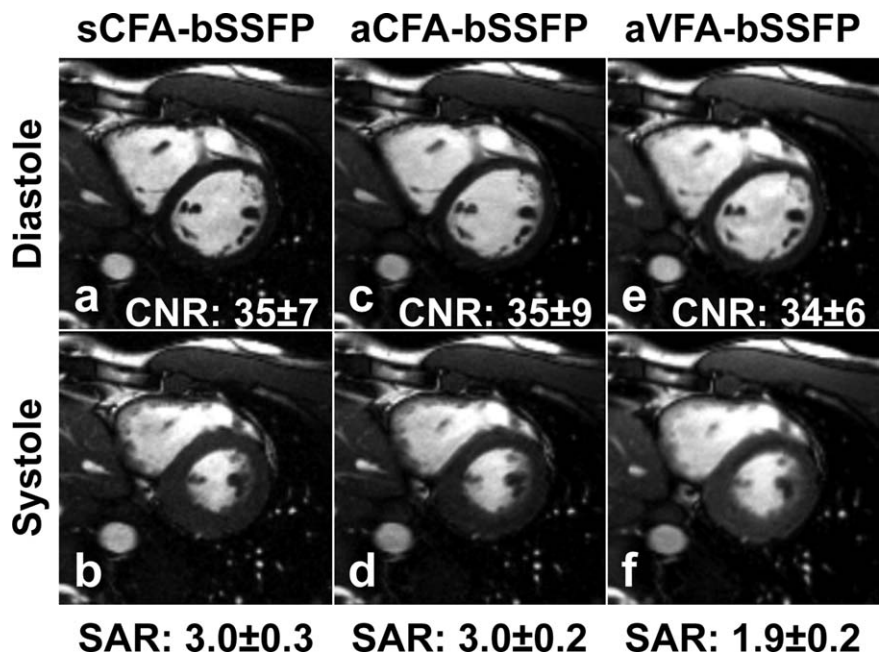

FIG. 7. Diastolic (top row) and systolic (bottom row) images of a volunteer acquired with conventional sCFA-bSSFP (**a, b**) of 70°, aCFA-bSSFP (**c, d**) of 70° and 30_70_40_80 aVFA-bSSFP (**e, f**) scheme. aVFA-bSSFP has blood-myocardium CNR similar to aCFA-bSSFP (34 ± 6 vs. 35 ± 9, $P = 0.5$) with reduced SAR (1.9 ± 0.2 vs. 3.0 ± 0.2 W/kg, $P < 10^{-10}$). The SAR and CNR of the sCFA-bSSFP were similar to aCFA-bSSFP experiments (3.0 ± 0.3 W/kg, 35 ± 7).

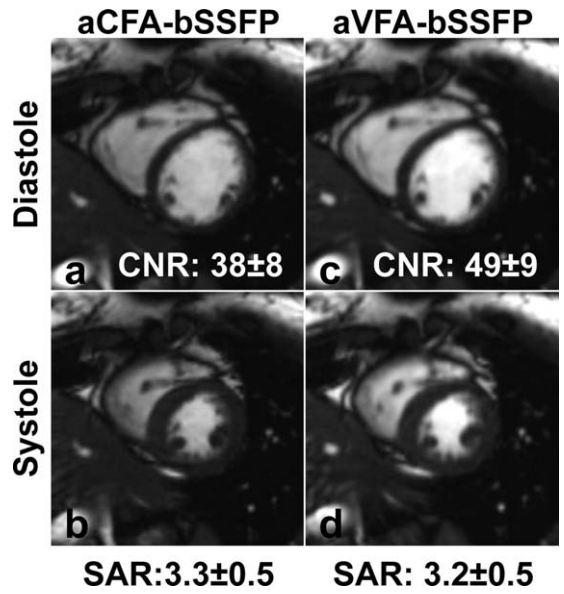

FIG. 8. Diastolic (top row) and systolic (bottom row) images of a volunteer acquired with aCFA-bSSFP (**a, b**) of 70° and 50_98_40_40 aVFA-bSSFP (**c, d**) scheme. aVFA-bSSFP has improved blood-myocardium CNR compared to aCFA-bSSFP (49 ± 9 vs. 38 ± 8, $P < 10^{-4}$) with similar SAR (3.2 ± 0.5 vs. 3.3 ± 0.5 W/kg, $P = 0.6$).

accommodates a higher effective FA. This may prove especially useful for cardiac cine imaging at 3 T where the FA is typically SAR-limited, which results in lower than desired CNR; or facilitate higher CNR at 1.5 T for more easier analysis of cardiac function.

Bloch simulations and the in vivo results show that aVFA-bSSFP can produce myocardial and blood signal similar to aCFA-bSSFP imaging while significantly reducing SAR and only slightly broadening the FWHM. The myocardial and blood signal simulations and in vivo myocardial and blood SNR results agree well. The current aVFA-bSSFP sequence does not accommodate parallel imaging, but the principles described herein are compatible with parallel imaging. When using parallel imaging, the percent SAR reduction accorded by using aVFA-bSSFP will be less than when we do not use parallel imaging.

The different parameters for the aVFA-bSSFP scheme should be chosen carefully for cardiac cine imaging. The blood SNR of the aVFA-bSSFP scheme is strongly dependent on α_{high}. For example, two different VFA schemes with constant α_{high}, but variable N_{high}, N_{ramp}, and α_{low} such as 10_70_40_100 and 30_70_20_80 (Fig. 9) have similar ventricular blood SNR due to the strong dependence on α_{high}. Hence, α_{high} should be chosen based on the desired blood-myocardium CNR (higher α_{high} produces greater CNR).

Lower N_{high} and lower N_{ramp} pulses with low α_{low} reduces the SAR, but increases the image blurriness (e.g., 10_70_20_40 vs. 10_70_40_80, Fig. 5a,b). Furthermore, if N_{ramp} is too low ghosting artifacts (13) will arise due to the residual signal oscillations during transition between the low and high steady states. Therefore, image blurriness and ghosting artifacts determine the lower bound on the acceptable N_{ramp} and N_{high}. Nonlinear ramp trajectories such as a Kaiser–Bessel trajectory (14) could also be used to reduce signal oscillations during the transition between steady states while ramping from α_{low} to α_{high}, but initial results (not shown) indicate only minimally observable differences for $N_{ramp} \geq 20$. The upper bound of the N_{ramp} and N_{high} depends on the desired SAR reduction and image blurriness. For example, two VFA schemes with different N_{high} and N_{ramp} such as 10_70_20_100 and 10_70_40_80 have similar blood-myocardium CNR and similar phantom image blurriness, but increased SAR of 1.69 vs. 1.62 W/kg, respectively.

Lower α_{low} increases the image blurriness, but decreases the total acquisition SAR. For example, the VFA schemes 10_70_20_40 and 30_70_20_40 have measured phantom image blurriness of 18.6 vs. 11.4, simulated FWHM of 2.4 vs. 1.32, and SAR of 0.21 vs. 0.32 W/kg, respectively. Hence, α_{low} should be chosen carefully such that the image blurriness is within acceptable limits for the overall reduction in SAR. Our experiments were performed with constant $N_{ky} = 204$. The dependence of the VFA scheme parameters on the image blurriness and SNR should be considered even for experiments with different phase resolution (N_{ky}). The aVFA-bSSFP

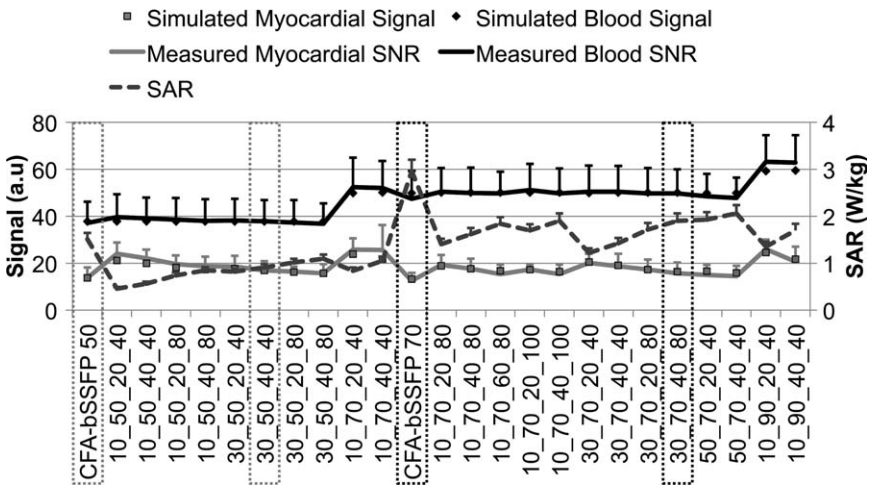

FIG. 9. Measured myocardial (gray solid line) and blood (black solid line) SNR from diastolic images for 25 different aCFA-bSSFP and aVFA-bSSFP sequences agrees well with the simulated stationary myocardial (gray squares) and flowing blood (black diamonds). The SAR (dashed line) for each sequence is also shown. The black dotted rectangles highlight the comparison of the CFA-bSSFP 70 with its corresponding 30_70_40_80 VFA-bSSFP scheme. The gray-dotted rectangles highlight the comparison of CFA-bSSFP 50 and its corresponding 30_50_40_40 VFA-bSSFP scheme.

cardiac cine imaging did not use preparation pulses to catalyze the sequence to steady state. However, preparation pulses like Kaiser–Bessel (15) can be used to further reduce the preparation duration and overall SAR of the sequence.

The results from Figures 9 and 5a show that the 30_50_40_40 aVFA-bSSFP scheme produces the least difference in blood-myocardium CNR compared to aCFA-bSSFP of 50° (21 ± 6 vs. 23 ± 5) with a minimal increase in the FWHM to 1.2 and SAR reduced by 40% (0.9 ± 0.1 vs. 1.5 ± 0.1 W/kg). The 30_70_40_80 aVFA-bSSFP scheme produces the least difference in blood-myocardium CNR compared to aCFA-bSSFP of 70° (34 ± 6 vs. 35 ± 9) with minimal increase in FWHM to 1.3 and maximum reduction in SAR of 36% (1.9 ± 0.2 vs. 3.0 ± 0.2 W/kg).

Low SAR imaging is important in patients with implanted devices such as pacemakers and ICDs to reduce the heating at the lead tip that could damage the surrounding tissue (16). aVFA-bSSFP (30_70_40_80) can reduce the SAR by 36% compared to sCFA-bSSFP (70°) cardiac cine imaging, while maintaining SNR and CNR and largely preserving resolution. Further simulation and experiments need to be performed to optimize the aVFA-bSSFP scheme parameters to produce blood-myocardium CNR similar to sCFA-bSSFP while maximizing SAR reduction and minimizing image blurring.

Limitations

The aVFA-bSSFP sequence uses an asynchronous k-space acquisition. The asynchronicity provides acquisition of all k_y-lines during all cardiac phases. For example, if the TR = 4 ms, $N_{ky} = 180$ (TR•$N_{ky} = 720$ ms) and RR-interval = 800 ms, 10 cardiac phases can be acquired uniformly in 9 RR-intervals. If, however, TR = 4 ms, $N_{ky} = 200$ (*T*R•$N_{ky} = 800$ ms) and RR-interval = 800 ms, then the k-space acquisition and cardiac cycle are synchronous and the same k-space line will be acquired for each point in the cardiac cycle. Hence, only one cardiac phase can be reconstructed. This is also equivalent to acquiring synchronously the same single-shot image for each cardiac cycle. However, in practice due to changes in the RR-interval during image acquisition, each cardiac phase may not be sampled uniformly. As a result, certain cardiac phases may be oversampled and the other cardiac phases may be under-sampled. Further developments and experiments are needed to refine techniques to uniformly sample k-space for all the cardiac phases.

The image blurriness was measured in the phantom images using the line profile along the phase encoding direction. These measurements agreed well with the simulation measurements of the FWHM of the PSF (Fig. 5). However, similar measurements such as septal sharpness (12) over diastolic images did not result in significant differences between the aVFA-bSSFP and aCFA-bSSFP schemes due to poor alignment of the myocardial septum with the phase encoding direction and other concomitant sources of blurring.

CONCLUSIONS

aVFA-bSSFP can be used for: (1) low SAR (at least 36% lower) cardiac cine imaging with similar blood-myocardium CNR compared to the conventional sCFA-bSSFP imaging or (2) high CNR (at least 28% higher) cardiac cine imaging with similar SAR compared to aCFA-bSSFP imaging, while nearly maintaining spatial resolution. aVFA-bSSFP may prove useful for cardiac structural and functional imaging in patients with implanted devices, three-dimensional imaging, real time imaging, high-field imaging, and any cardiac cine application, that is, SAR limited.

ACKNOWLEDGMENTS

The authors are grateful for research support from Siemens Medical Systems.

REFERENCES

1. Finn JP, Nael K, Deshpande V, Ratib O, Laub G. Cardiac MR imaging: state of the technology. Radiology 2006;241:338–354.
2. Markl M, Pelc NJ. On flow effects in balanced steady-state free precession imaging: pictorial description, parameter dependence, and clinical implications. J Magn Reson Imaging 2004;20:697–705.
3. Hennig J, Weigel M, Scheffler K. Multiecho sequences with variable refocusing flip angles: optimization of signal behavior using smooth transitions between pseudo steady states (TRAPS). Magn Reson Med 2003;49:527–535.
4. Busse RF, Hariharan H, Vu A, Brittain JH. Fast spin echo sequences with very long echo trains: design of variable refocusing flip angle schedules and generation of clinical T2 contrast. Magn Reson Med 2006;55:1030–1037.
5. Paul D, Markl M, Fautz H-P, Hennig J. T2-weighted balanced SSFP imaging (T2-TIDE) using variable flip angles. Magn Reson Med 2006; 56:82–93.
6. Srinivasan S, Gilson WD, Flammang A, Paul D, Patil S. Fast, low SAR and off-resonance insensitive T2 weighted variable amplitude PSIF (T2 VAPSIF) imaging. In Proceedings of the 20th Annual Meeting of ISMRM, Melbourne, Australia, 2012. p. 290.
7. Worters PW, Hargreaves BA. Balanced SSFP transient imaging using variable flip angles for a predefined signal profile. Magn Reson Med 2010;64:1404–1412.
8. Paul D, Zaitsev M. Improved SNR in linear reordered 2D bSSFP imaging using variable flip angles. Magn Reson Imaging 2009;27:933–941.
9. Stehling MK. Improved signal in "snapshot" FLASH by variable flip angles. Magn Reson Imaging 1992;10:165–167.
10. Kellman P, Chefd'hotel C, Lorenz CH, Mancini C, Arai AE, McVeigh ER. High spatial and temporal resolution cardiac cine MRI from retrospective reconstruction of data acquired in real time using motion correction and resorting. Magn Reson Med 2009;62:1557–1564.
11. Schär M, Kozerke S, Fischer SE, Boesiger P. Cardiac SSFP imaging at 3 tesla. Magn Reson Med 2004;51:799–806.
12. Larson AC, Kellman P, Arai A, Hirsch GA, McVeigh E, Li D, Simonetti OP. Preliminary investigation of respiratory self-gating for free-breathing segmented cine MRI. Magn Reson Med 2005;53:159–168.
13. Paul D, Hennig J. Comparison of different flip angle variation functions for improved signal behavior in SSFP sequences. In Proceedings of the 12th Meeting of ISMRM, Kyoto, Japan, 2004. p. 2663.
14. Busse RF. Reduced RF power without blurring: correcting for modulation of refocusing flip angle in FSE sequences. Magn Reson Med 2004;51:1031–1037.
15. Le Roux P. Simplified model and stabilization of SSFP sequences. J Magn Reson 2003;163:23–37.
16. Langman DA, Goldberg IB, Finn JP, Ennis DB. Pacemaker lead tip heating in abandoned and pacemaker-attached leads at 1.5 tesla MRI. J Magn Reson Imaging 2011;33:426–431.